



A Case Study on the Progressive Failure Mechanism of I-180 Slope Using Numerical and Field Observations

Binyam Bekele, Ph.D. candidate, Department of Civil and Environmental Engineering, University of Nebraska-Lincoln, Lincoln, NE; email: bbekele@huskers.unl.edu

Chung Song, Associate Professor, Department of Civil and Environmental Engineering, University of Nebraska-Lincoln, Lincoln, NE; email: csong8@unl.edu

Mark Lindemann, Roadway Asset Management Engineer, Materials and Research Division, Nebraska Department of Transportation, Lincoln, NE; email: mark.lindemann@nebraska.gov

ABSTRACT: A progressive failure of shallow slopes is commonly encountered in eastern Nebraska due to the region's unique geological and weather conditions. This study presents a case study for a slope in Nebraska that experienced a progressive failure. Emphasis was given to examine the condition and triggering mechanisms of the slope failure through a field observation and numerical modeling. FLAC2D was employed to conduct the numerical simulation of the progressive failure based on a hydromechanical coupled framework. Data from experimental test results were utilized to model the mechanical behavior of the soils. The progressive development of the slip surface, degradation of shear strength parameters, slope displacement, and variation of the local factor of safety with time were analyzed. A similar outcome from the numerical analysis to that of the field observations demonstrated how various strength degradation mechanisms could be integrated into a single numerical analysis to understand the progressive failure of shallow slopes.

KEYWORDS: Progressive failure, hydromechanical framework, strength degradation, weathering; strain softening

SITE LOCATION: [Geo-Database](#)

INTRODUCTION

Slope failures are commonly encountered in eastern Nebraska and neighboring states along the federal, state, and county highways (Eversoll 2013). These failures have brought damage to nearby roadways, homes, and utility lines. Apart from the physical damage, retrofitting activities have imposed significant costs to the local transportation authority. Consequently, various research is being conducted to characterize the failure mechanisms and develop an economical and sustainable means of retrofitting failed slopes (e.g., Bitar 2020; Song et al. 2019).

Most of the slope failures are shallow and exhibit a progressive movement. A progressive failure is characterized by gradual propagation of the slip surface from a localized failed zone (Leroueil 2001; Mesri and Shahien 2003; Skempton 1964; Take and Bolton 2011). The initiation of a local failure may be attributed to a non-uniform stress distribution and localized reduction of the shear strength of slope materials (Darban et al. 2019; Potts et al. 1997; Skempton 1964). In eastern Nebraska, the localized strength reduction may be attributed to the geological nature of the soils, the weathering effect due to wet-freeze-thaw cycles, and the action of water (Bitar 2020; Eversoll 2013; Song et al. 2019). The typical geology of eastern Nebraska consists of loess, glacial tills, and shales from top to bottom (Song et al. 2020). Loess contains inter-particle cementations that can be significantly weakened upon saturation (Parsons et al. 2009). Glacial tills and shales may show strain-softening behavior (Carse 2014; Song et al. 2019). Shales occasionally contain high content of expansive soils, and glacial tills may contain up to 10% of expansive soils (Botts 1998; Song et al. 2019). Moreover, open fissures in shales and glacial tills may facilitate the infiltration of water and weathering-induced degradation of shear strength (Alonso and Pineda 2006; Bitar 2020). Recently, Bitar (2020) reported up to 45% shear strength reduction due to weathering in glacial tills based on a direct shear test. Botts (1998) also reported shales may exhibit up to 80% strength reduction due to slaking based on a triaxial compression test.

Submitted: 15 December 2020; Published: 10 December 2021

Reference: Bekele B., Song C., and Lindemann M. (2021). A Case Study on the Progressive Failure Mechanism of I-180 Slope Using Numerical and Field Observations. International Journal of Geoengineering Case Histories, Volume 7, Issue 1, pp. 1-21, doi: 10.4417/IJGCH-07-01-01

This study examined the failure condition and triggering mechanisms for a failed slope in Lincoln, Nebraska, U.S.A. Furthermore, a transient hydromechanical slope stability analysis was conducted by incorporating potential contributing factors of the failure such as strain softening, weathering, and rainfall infiltration simultaneously. The numerical analysis was aimed at performing a deformation analysis and to help understand the nature of progressive failure in terms of the gradual propagation of slip surface and variation of a local factor of safety with time. FLAC2D, which is based on a two-dimensional explicit finite difference method, was used to model the problem. The effect of strain softening and weathering were incorporated in the mechanical constitutive model by using user-defined functions, while the effect of rainfall infiltration was accounted for using an unsaturated flow formulation.

DESCRIPTION OF THE FAILED SLOPE

Location and Geometry

The failed slope considered in this study is in the city of Lincoln, Nebraska, U.S.A., as shown on the map in Figure 1(a). Specifically, it is located in the northern part of the city and at the intersection between Interstate-180 (I-180) and Superior Street. The plan view of the slope is shown in Figure 1(b). The failed zone (slide area) has a substantial spatial coverage with a maximum transversal width of about 40 m and a longitudinal length of about 22 m. Adjacent to the toe of the slope, there is a ramp for merging traffic into I-180 as shown in Figure 1(b).

The slope was constructed in 1964. It was formed from a sizeable cut section from the natural condition. Unfortunately, the authors could not retrieve the original geometry of the slope. However, the best estimate of the initial slope geometry was back analyzed from a recently conducted LiDAR survey (in 2012) and total station-based field surveying (in 2018). Figure 2(a&b) shows the topographic contour plots obtained from the LiDAR and field surveying, respectively. Based on these contour maps, the initial two-dimensional (2D) profile of the slope was estimated, and Figure 2(c) shows the estimated initial profile and the deformed slope profile for 2012 and 2018 based on LiDAR and field surveying, respectively. The 2D representation was taken at a place where the contour is symmetric, as shown by the broken section line in Figure 2(a&b). The projected initial profile had a slope of 3:1 with a height and width of 8.8 m and 26.4 m, respectively.

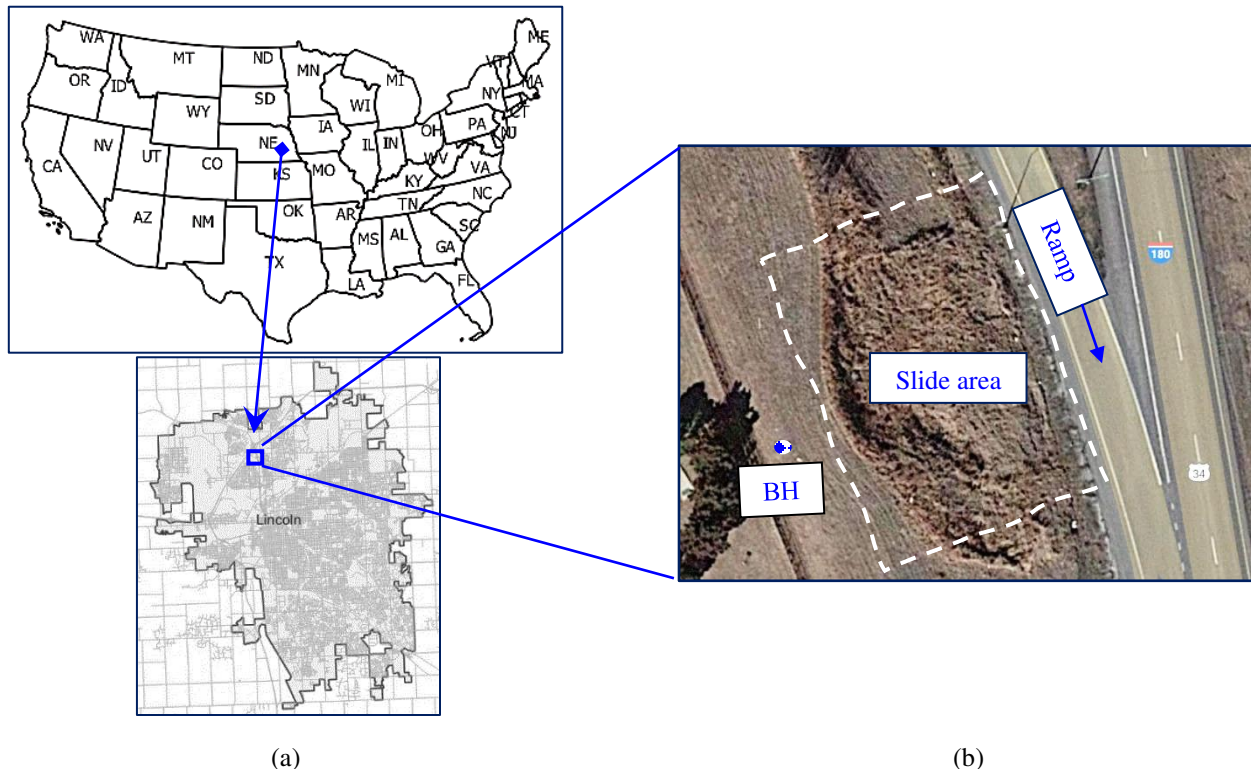


Figure 1. (a) Location of the failed slope site, and (b) plan view of the slope (2020) (note: BH is to mean borehole).

Description of the Failure Condition

The failure of the slope had begun in 1996-1997. This means it had a long-term stability problem as it took about 32-33 years for failure to happen. A recent observation made from visual inspection and images from Google was used to describe the slope's failure condition. Figure 3 shows the surficial condition of the slope at various times (2012 to 2019). In all cases, it is observed that the failure zone did not extend to the crest of the slope and appeared to have a crown somewhere on the slope itself. The crown of the failed zone had potentially developed from an initial tension crack due to the tendency of the unstable zone to detach from the stable zone. The stable zone above the crown had an almost unnoticeable deformation and seemed to be intact, as shown in Figure 3. This claim is also supported by slope surface deformation patterns obtained by LiDAR and field surveying, as shown in Figure 2(c). A scarp was formed, and soil was exposed due to continued slope movement (see Figure 3; image taken in July 2019). Moreover, the pavement adjacent to the slope toe had no visible distress induced by the slope failure as per a visual observation.

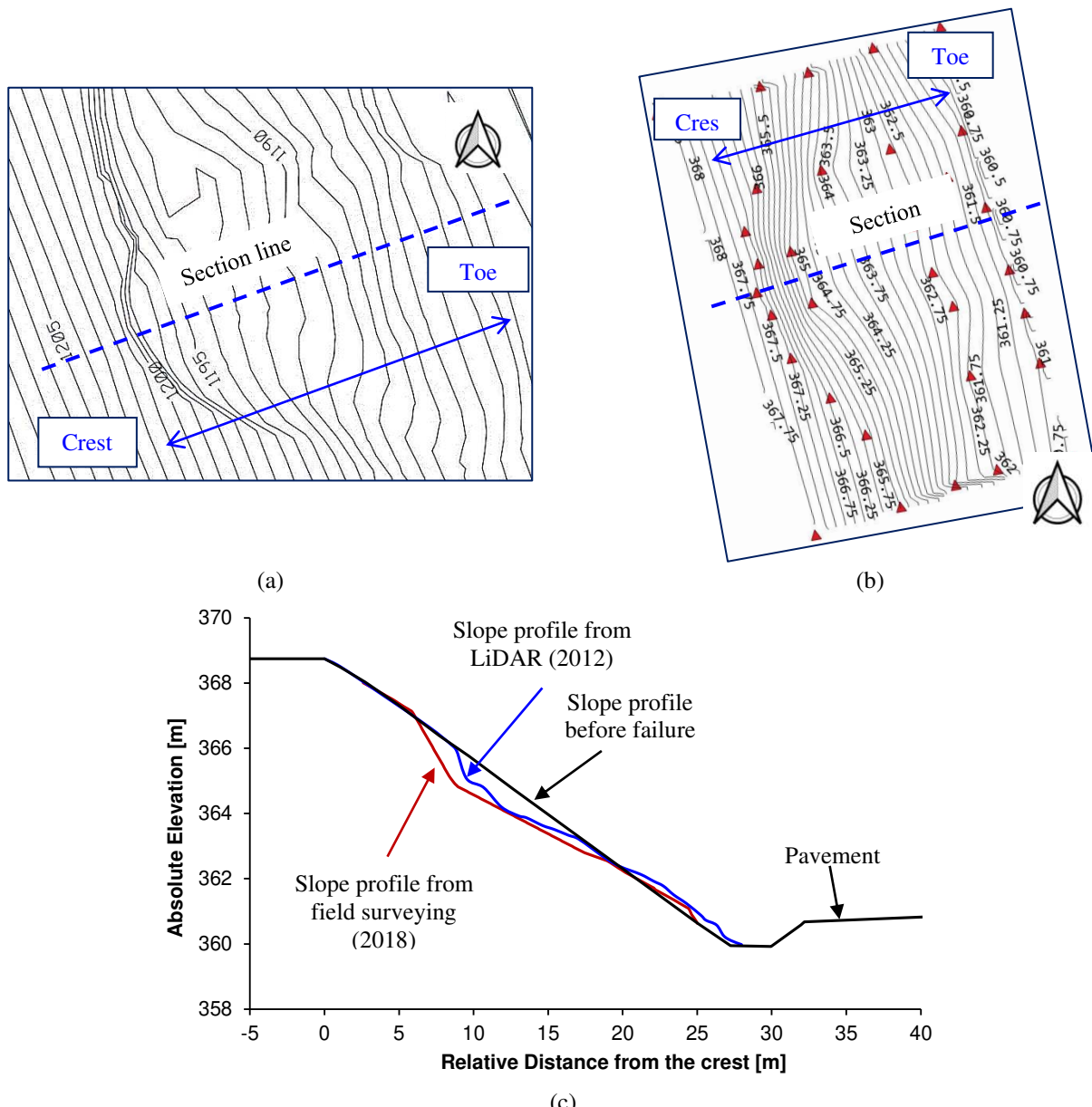


Figure 2. (a) Topographic contour plot from LiDAR (in 2012), (b) topographic contour plot from field surveying using a total station. (Note: Contour labels are elevations. The units are in feet for the LiDAR contour. The units are in meters for the field surveying contour. The red triangles in Figure (b) elucidate the location of surveying pegs.)

There had been no engineered “official” repair work conducted on the slope. However, there were a few “maintenances” performed. The maintenance work involved adding some fill material over the failed zone and repairing the face of the slope, as shown in Figure 3 (see the image taken on May 2013). However, the slope restored the observed failure condition after the “repairs” (see the image taken in July 2013 and after). The recurrence of failure suggested that the slip surface may be located below the zone of “repair”.

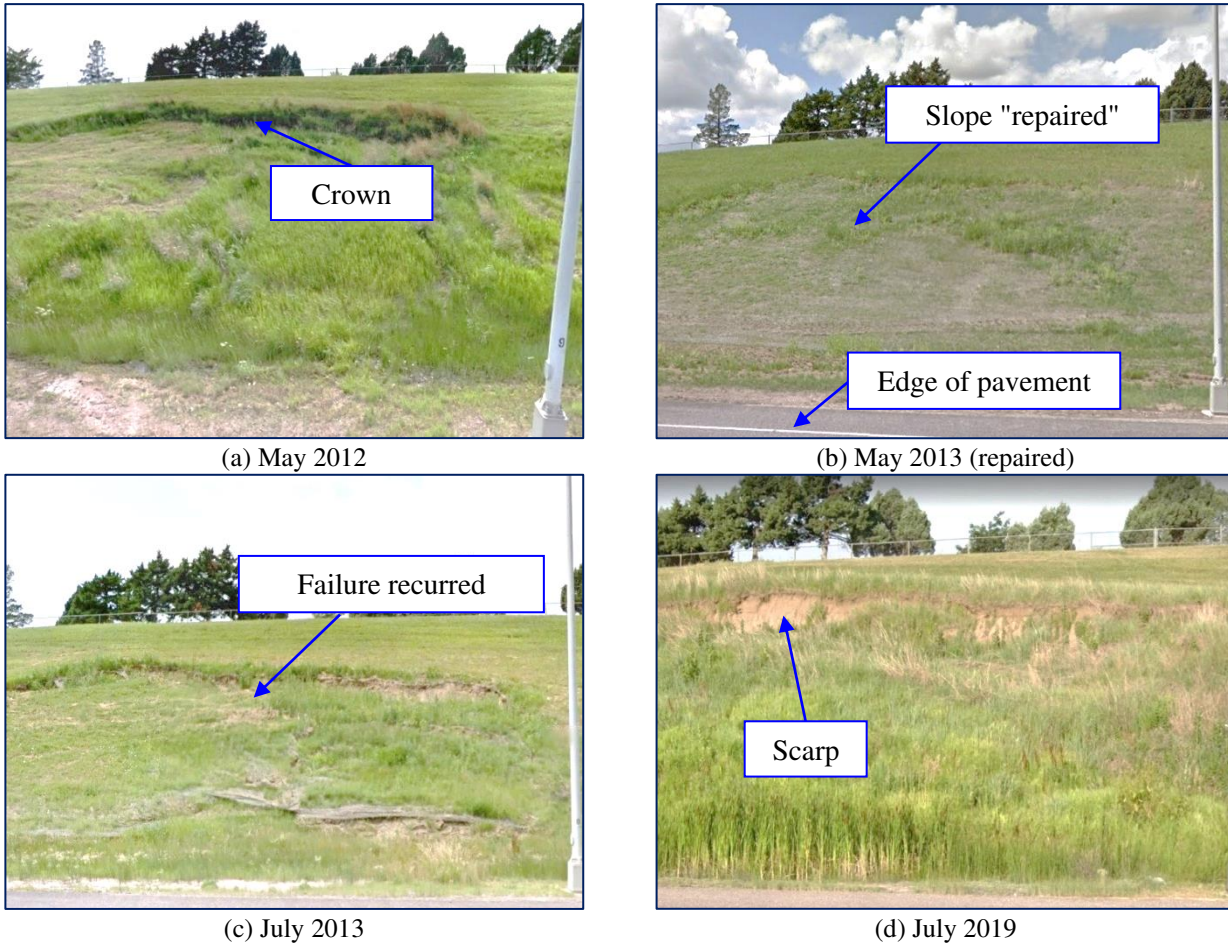


Figure 3. Images depicting the failure condition of the slope (From 2012 to 2019).

DESCRIPTION OF THE GEOTECHNICAL CHARACTERISTICS

Soil Stratification

A borehole (BH) was drilled at the crest of the slope, as shown in Figure 1. The depth of the borehole extended up to 8 m, which was close to the height of the slope. Six Shelby tubes (designated as S1 to S6) were recovered, and some portion of the recovered undisturbed soil samples were used for strength characterization, while the remaining portion was utilized to perform index tests such as gradation (ASTM International D6913 2017; ASTM International D7928 2017) and Atterberg limits tests (ASTM International D4318 2017). Figures 4 and 5 present the grain size distribution and the details of these soil layers, their classification, and Atterberg limits, respectively.

The first two Shelby tubes (S1 and S2) showed similar behavior and were designated as Layer-1. The parent material for this layer was categorized under the Peoria Loess formation. This uppermost layer is abundant in Nebraska (Arthur Bettis et al. 2003; Song et al. 2020). It consisted of predominantly fine particles. The Atterberg result showed the soil had medium plasticity. The unified soil classification and textural classification (USCS) of the layer is shown in Figure 5. The underlying layer, which is designated as Layer-2, was identified from the Shelby tube S2. The visual identification, as well as the gradation test result shown in Figure 4, depicted how the soil was uniformly graded and predominantly composed of fine

sand particles. The soil had almost no cohesion (NP material). Moreover, USCS soil classification indicated the layer was poorly graded sand with silt (SP-SM).

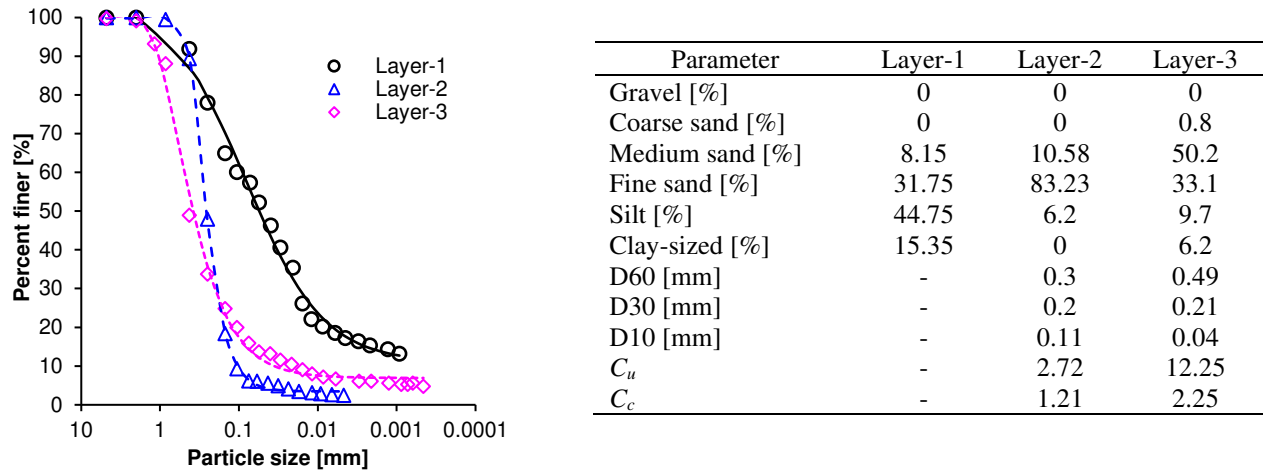


Figure 4. Grain size distribution of the soil layers and proportions of various size ranges. (Note: D60, D30, and D10 are particle sizes corresponding to 60%, 30%, and 10% finer, respectively. C_u and C_c are coefficient of uniformity and curvature, respectively.)

Samples from S4, S5, and S6 showed an identical visual and index properties layer, and were designated as Layer-3. The parent material for this layer corresponded to the glacial till formation, which is also a typical geological formation beneath loess formation in eastern Nebraska (Song et al. 2020). It consisted of larger-sized sand particles, as depicted in Figure 4. However, it also contained considerable fines of 16% (which is > 12%). The Atterberg limits test on these fines showed marginal behavior between medium and high plasticity. The ratio of the plasticity index (PI) to the clay content indicated the soil had higher activity (expansion potential), which was about 3.5. The USCS and textural classifications of the indicated soils were clayey sand (SC) and loamy sand, respectively. Groundwater table was not observed during the drilling operation, suggesting it is below 8 m deep.

Depth (m)	Graphic log	Soil description and classification	Sample	Moisture Content	Dry unit Weight (kN/m ³)	LL(%) PI(%)
2.0		Slightly moist and composed of mostly fine particles.	S1			
		USCS: clay with medium plasticity (CL). Textural classification: Loam	S2	13.2 %	13.25	43.6 21.2
4.0		Dry, tan color, and composed of fine sands with small silt content. USCS: poorly graded sand with silt (SP-SM). Textural classification: Sand.	S3	3.8%	13.30	NP
		Moist, gray/orange color glacial till composed of mostly medium to fine sandy materials with clay. The activity of the clay mineral is 3.70. USCS: clayey sand (SC). Textural classification: Loamy sand	S4 S5 S6	18% 31% 31%	14.50	48.85 23.80
6.0						
8.0						
10.0						

Figure 5. Borehole log and description of the soil conditions (note: LL is the liquid limit, PI is the plasticity index, NP means non-plastic, and USCS refers to unified soil classification system).

Strength Characteristics

Isotropically consolidated drained (CD) triaxial tests (ASTM International D7181 2011) were conducted on undisturbed soil specimens. Triaxial specimens were prepared for Layer-1 and Layer-3 soils. However, it was difficult to prepare a triaxial sample for Layer-2 soils. CD tests were conducted under a saturated condition. The drainage systems (pumps and tubing) and specimens were saturated by allowing water to flow through. A backpressure saturation was conducted using a back pressure of 345 kPa and 450 kPa on Layer-1 and Layer-3 specimens, respectively, to dissolve any air remaining in the specimen voids. After a saturation check, the specimens were consolidated using the target confining stress level (cell pressure). The shearing stage was conducted under a drained condition and with a controlled strain rate. The strain rate was selected following a recommendation by ASTM International D7181 (2011). The drained tests were conducted under two distinct levels of confining stresses. The confining stresses were selected to mimic shallow depth for the anticipated shallow failure condition. Figure 6(a, b) shows the shear stress (deviatoric) versus axial strain plots for Layer-1 and Layer-3 soils with the confining stresses shown in the keys. In addition, Figure 6(c, d) shows the volumetric strain versus the axial strain relationship for Layer-1 and Layer-3 soils. The elastic modulus of the soils slightly increased as the confining stress was increased. From Figure 6(a, b), it is observed that the shear strength of the soils became higher for higher confining stress in both layers. Layer-3 specimen showed a strain softening behavior at a lower confining stress level, as shown in Figure 6(b). At a higher confining stress level, the specimen showed a peak shear strength without a tendency of softening. Looking at the volumetric strain vs. axial responses, the specimen from Layer-1 showed a contraction behavior for both levels of confining stresses, as shown in Figure 6(c). On the other hand, specimen from Layer-3 showed a dilation behavior under a lower confining stress level and contraction behavior under a higher confining stress level.

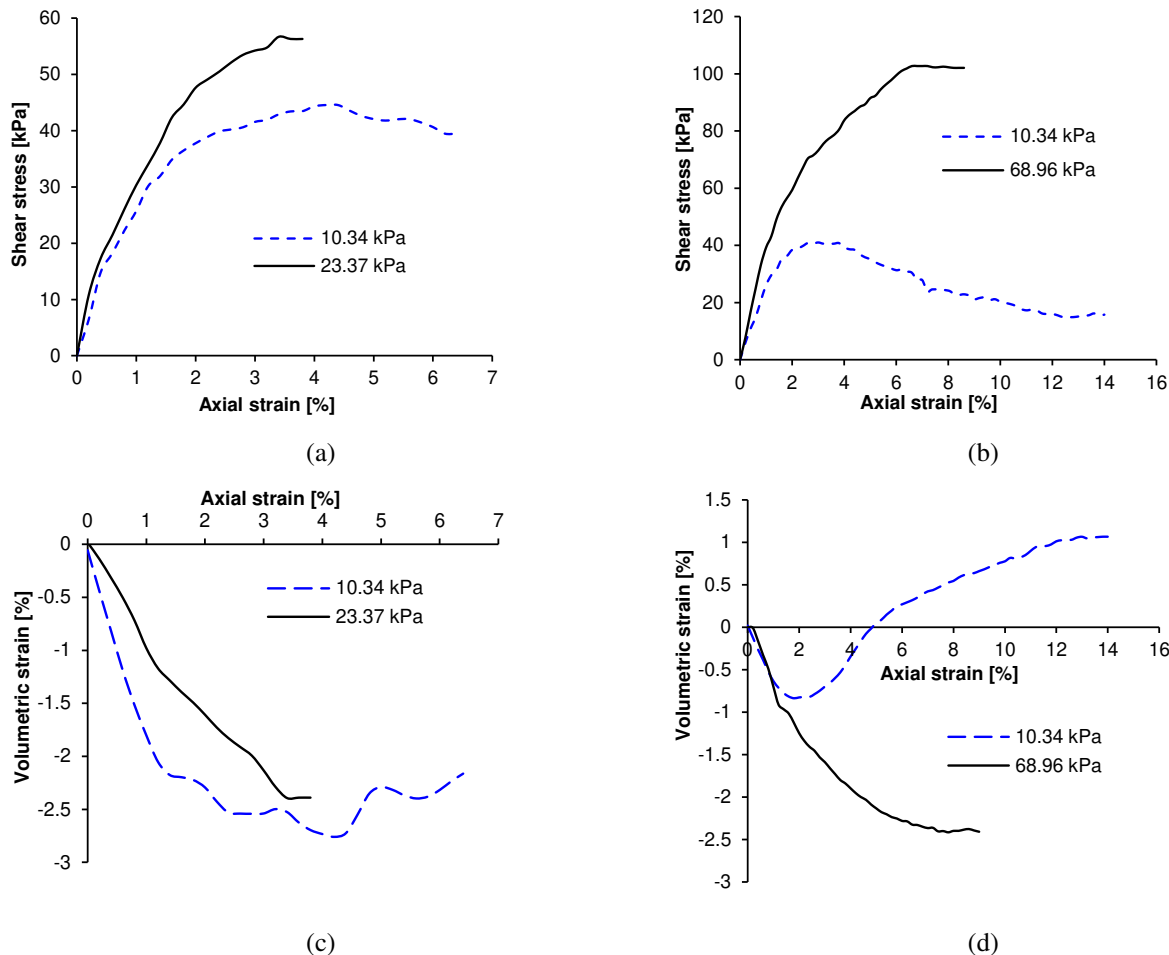


Figure 6. Isotropically consolidated drained triaxial test results: (a) shear stress vs. axial strain for Layer-1, (b) shear stress vs. axial strain for Layer-3, (c) volumetric strain vs. axial strain for Layer-1, and (d) volumetric strain vs. axial strain for Layer-3 (note: numbers in the legends are confining stresses used).

The stiffness and strength behavior of Layer-2 soils were evaluated from a cone penetration test (CPT). The penetration was conducted at the standard speed of 2 cm/s. The test was conducted up to a depth of 4 m. The relevant result from the cone penetration test result is shown in Figure 7. Based on the test, the cone tip resistance (q_c) of Layer-2 soils was found to be higher than the adjacent soil layers, which is typical for sandy soils (Dagger et al. 2018). The average cone tip resistance of the layer was found to be 14 MPa

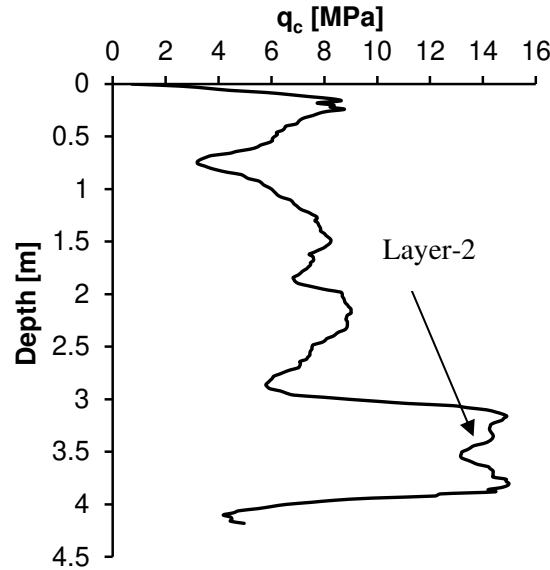


Figure 7. Cone tip resistance versus depth.

Weathering Behavior of Glacial Tills

Weathering is one of the anticipated failure mechanisms that may have contributed to the failure of the slope. A recent study by Bitar (2020) reported that glacial tills may demonstrate weathering-induced strength degradation. The soils considered by the study share some similarities to Layer-3 soils in terms of common geological history and close geographical proximity. Therefore, findings reported in Bitar (2020) were projected to describe the weathering-related geotechnical behavior of Layer-3 soils. For the purpose of completeness, the weathering test procedure and test results reported are briefly discussed. Figure 8 shows the equipment used in the weathering test.

First, glacial till specimens were compacted in a compaction mold adopted from Sullivan et al. (2015), as shown in Figure 8(a). The soils were compacted to their maximum dry density (1.64 g/cm^3) and optimum moisture content (18%) as determined from a standard proctor compaction test (ASTM International D698 2012). Then, compacted soils were trimmed into small PVC molds and secured with two porous stones at the top and bottom, as shown in Figure 8(b). Next, specimens in the PVC molds were subjected to the action of weathering. Initially, they were placed in a water bath at room temperature for about 24 hours, then transferred into a freezer at -21°C and kept for another 24 hours. Following that, they were thawed in an oven at 75°C for again 24 hours. The wet-freeze-thaw cycles were repeated 2, 4, and 8 times to simulate various levels of weathering. At the end of the set weathering cycles, the shear strengths of the weathered samples were determined using a direct shear test (ASTM International D3080 2004). A normal stress of 20 kPa was adopted to closely represent a shallower depth condition. A shear displacement rate of 0.25 mm/min was used during the test. Interested readers may find more details about the test procedure in Bitar (2020).

Figure 9(a, b) shows test findings from Bitar (2020). The peak strength decreased as the number of weathering cycles increased from 0 to 8 cycles, demonstrating that weathering has a destructive potential on the shear strength. The reduction of the peak shear strength and the associated percentage reduction is plotted as a function of weathering cycles in Figure 9(b). A nonlinear strength reduction was observed. A significant strength degradation was also observed going from 0 to 2 cycles (~30% reduction) as compared to the reduction observed when moving from 4 to 8 cycles (~7% reduction in strength).

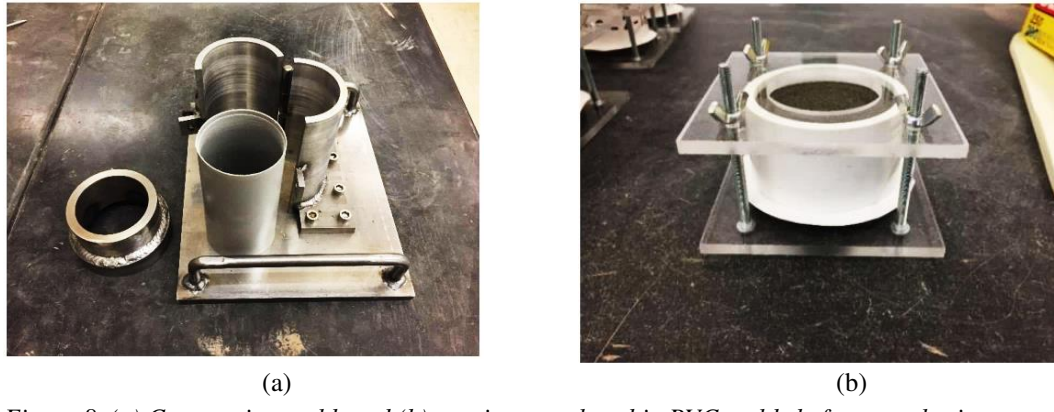


Figure 8. (a) Compaction mold, and (b) specimen enclosed in PVC molds before weathering.

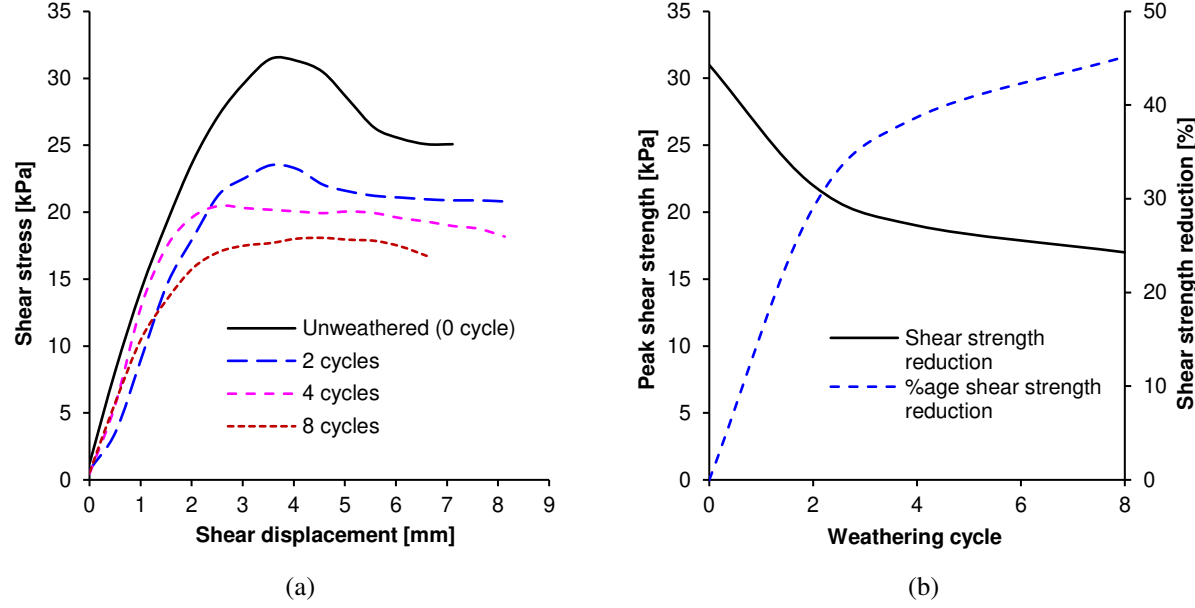


Figure 9. Weathering test results by Bitar (2020): (a) shear stress vs. shear displacement for different weathering cycles, and (b) peak shear strength and the percentage reduction with weathering cycles.

NUMERICAL MODELING OF THE SLOPE

Numerical modeling was performed to understand the progressive failure from a computational perspective. The anticipated failure mechanisms of strain softening, weathering, and rainfall infiltration were incorporated using a hydromechanical coupled transient analysis. However, it is noted that the transient analysis did not simulate the exact timescale of the slope (i.e., from 1964 to the present) due to the uncertainties related to the initial conditions (geometry and effective stress), infiltration rate over the years, evaporation, and the actual rate of weathering. Therefore, the numerical simulation only sought to demonstrate the time-dependent progressive failure of the slope based on average conditions such as average rainfall data over many years and an assumed rate of weathering.

The numerical modeling was performed using FLAC2D (Itasca Consulting Group, Inc. 2019). The pertinent governing equations were solved using an explicit finite difference method. The spatial domain of the problem was discretized into multiple zones using grids. The displacement and pore pressure were computed at the grid points (intersection of grid lines). A linear variation of variables was assumed within grid zones. A large-scale deformation was accommodated by adding the incremental displacements to the initial coordinates of the grid points as the simulation time progressed (Itasca Consulting Group, Inc. 2019). The time domain was discretized into small explicit time steps to ensure numerical stability. A stable

timestep was automatically computed and applied by FLAC. The theoretical framework, numerical model setup, and material parameters are discussed in the following sections.

The Theoretical Framework

Unsaturated Flow

The unsaturated flow process is formulated through the consideration of the mass balance of water. Ignoring source/sink terms, the unsaturated flow of a wetting-fluid (water) in a deformable porous media is given by (Itasca Consulting Group, Inc. 2019):

$$n \left[\frac{s}{K_w} \frac{\partial p}{\partial t} + \frac{\partial s}{\partial t} \right] = - \left[\frac{\partial q_i}{\partial x_i} + s \frac{\partial \varepsilon_v}{\partial t} \right] \quad (1)$$

where n is the porosity [dimensionless]; s is the degree of saturation [dimensionless]; K_w is the bulk modulus of water [FL^{-2}]; p is the pore-water pressure [FL^{-2}]; q is the volume flux of water [LT^{-1}]; and ε_v is the volumetric strain [dimensionless]. The volumetric strain represents the deformation of the porous solid skeleton. The time variation of the degree of saturation can be related to the pore pressure using a soil-water characteristics curve (SWCC) model. The SWCC model relates the matric suction to the degree of saturation (Lu and Likos 2004). The well-known SWCC curve by Van Genuchten (1980) is implemented in FLAC. This model is given by:

$$s_e = \frac{s - s_r}{1 - s_r} = [1 + (\alpha\psi)^n]^{-m} \quad (2)$$

where s_e is the effective saturation [dimensionless]; s_r is the residual saturation [dimensionless]; α is a fitting parameter that corresponds to the air-entry pressure [$(\text{FL}^{-2})^{-1}$]; n, m are fitting parameters which are interrelated using $m = 1 - \frac{1}{n}$ [both dimensionless]; and ψ is the matric suction [FL^{-2}] given by $\psi = p_a - p_w$, where p_a is the air pressure [FL^{-2}] and p_w is the pore water pressure [FL^{-2}]. The air pressure was considered atmospheric and taken 0 kPa. The volume flux in Equation (1) is computed using Darcy's law, as shown in Equation (3):

$$q_i = - \frac{k_{ij}}{\gamma_w} k_r \frac{\partial}{\partial x_j} (p - \rho_w g_k x_k) \quad (3)$$

where k_{ij} is the saturated hydraulic conductivity tensor [LT^{-1}]; k_r is the relative hydraulic conductivity function [dimensionless]; γ_w is the unit weight of water [FL^{-3}]; and ρ_w is the density of water [ML^{-3}]. An isotropic hydraulic conductivity was assumed for simplicity, i.e., $k_{ij} = k_{sat}$, where k_{sat} is the saturated hydraulic conductivity. k_r is obtained using the Van Genuchten-Mualem model (Van Genuchten 1980), as shown in Equation (4):

$$k_r = s_e^{0.5} [1 - (1 - s_e^{1/m})^m]^2 \quad (4)$$

Effective Stress-Strain Relationship

The Bishop's effective stress measure (Bishop 1959) was used to express the stress-strain relationships. This stress measure includes the effect of matric suction in a single stress variable as follows:

$$\sigma'_{ij} = \sigma_{ij} + \bar{p} \delta_{ij}, \text{ with } \bar{p} = \chi p_w + (1 - \chi) p_a \quad (5)$$

where σ'_{ij} is the effective stress tensor [FL^{-2}]; σ_{ij} is the total stress tensor [FL^{-2}]; χ is an effective stress parameter [dimensionless], and δ_{ij} is the Kronecker delta. χ is a function of the degree of saturation (Lu and Likos 2004). χ is assumed linearly proportional to the degree of saturation s_w in FLAC.

The elastic behavior of the soil layers was mimicked by the well-known Hooke's law:

$$\sigma'_{ij} = \lambda \varepsilon_{kk} \delta_{ij} + 2G \varepsilon_{ij}, \text{ with } \lambda = K - \frac{2G}{3} \quad (6)$$

where λ is the lame's parameter [FL^{-2}]; K is the bulk modulus [FL^{-2}]; G is the shear modulus [FL^{-2}]; and ε_{ij} is the strain tensor [dimensionless]. In this study, the bulk modulus was expressed as a function of confining stress using the Janbu's method as shown in Fellenius (2015):

$$K = K_B p_{ref} \left(\frac{\sigma'_3}{p_{ref}} \right)^\beta \quad (7)$$

where K_B is the bulk modulus number [dimensionless]; p_{ref} is reference pressure = 100 kPa; σ'_3 is the effective confining stress [FL^{-2}]; and β is a modulus exponent that depends on the type of soil [dimensionless]. β is lower for coarse-grained soils and higher for fine-grained soils (Fellenius 2015).

The plastic behavior of the soils was represented using the Mohr-Coulomb model. The failure criterion of this model is obtained as shown in Equation (8):

$$\frac{\sigma'_1 - \sigma'_3}{2} = \frac{(\sigma'_1 + \sigma'_3)}{2} \sin \phi' + c' \cos \phi' \quad (8)$$

where σ'_1 is effective major principal stress [FL^{-2}]; σ'_3 is effective minor principal stress [FL^{-2}]; c' is effective cohesion [FL^{-2}]; and ϕ' is the effective friction angle [degrees].

A general comment about the constitutive model is given as follows. For an unsaturated condition, the suction pressure increases the effective stress as per the Bishop's model. This produces an apparent cohesion term in the constitutive model. This term increases the shear strength of the soils. However, it will become lost when the soils become saturated due to rainfall infiltration. The effect of strain softening behavior and weathering degrade the shear strength parameters of the soils, and in turn, affect the size of the failure envelope in Equation (8). Therefore, the dynamics of the failure envelope were accounted for during the incorporation of these phenomena in the numerical modeling.

Model Setup, Initial, and Boundary Conditions

An optimal discretization was selected based on accuracy and computational efficiency. The boundaries of the domain were delineated as shown in Figure 10. The right, left, and bottom extents were selected as a function of the height of the slope, H , following a study by Rahardjo et al. (2000). The left and right boundaries were set to be rollers, and the bottom was fixed. A surcharge load of 12 kPa (for 0.6 m thick pavement with 20 kN/m³ average unit weight) was applied to simulate the pavement self-weight. For the water flow analysis, the left, right, and bottom boundaries were assumed impervious. The top surface was assumed free for drainage. A rainfall infiltration was applied on the surface of the slope and the ditch adjacent to the pavement. The groundwater table was placed at 15 m below the ground surface.

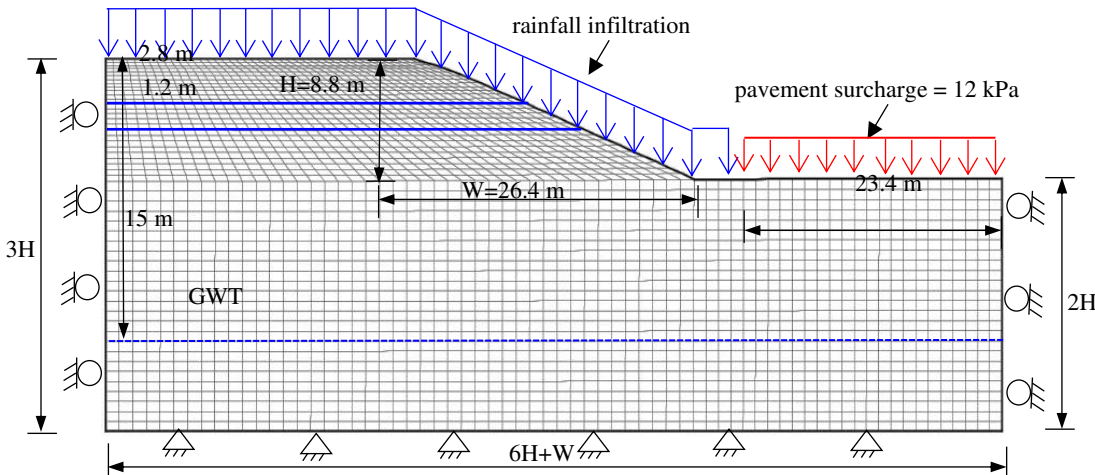


Figure 10. Model setup: geometry, grid discretization, boundary, and internal conditions.

The initial state of the slope before failure was assumed based on an engineering rationale. The pore pressure distribution was initiated based on the assumption of drier conditions during construction. Therefore, a near residual saturation condition was assumed for the soil above the groundwater table, with care being taken not to assign very high suction pressure. The assumed initial degree of saturation is shown in Table 1. The total stress condition was initiated based on an overburden (due to gravity) pressure distribution. The horizontal and vertical displacements are set at nearly zero by assuming a higher modulus during initialization.

Rainfall Infiltration

Rainfall infiltration was applied as a time-dependent boundary condition. The average infiltration rate for the Lincoln area was compiled from 20 years of metrological records (UNL 2020). The average monthly infiltration rate was computed by dividing the total monthly precipitation by the number of days in the month. Figure 11 shows the averaged infiltration rate for a year. The discrete average monthly infiltration rate shown in the bar graph was converted to a continuous Gaussian distribution type function, as shown in Figure 11.

The implementation of continuous function simplified the numerical modeling. The infiltration function was executed using a user-defined program in FLAC. The implementation of continuous function also created a continuous discharge into the slope and inducted a smooth variation of degree of saturation within the slope. However, this response deviates from the reality and therefore it was noted as one of the limitations of continuous rainfall assumption despite its simplicity in the numerical application.

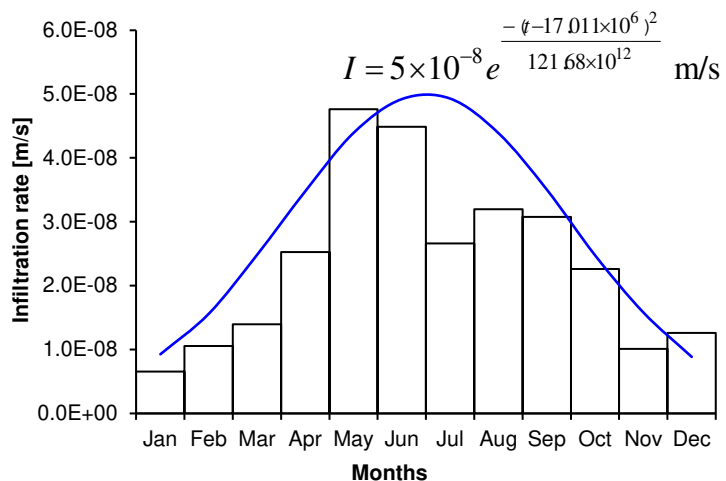


Figure 11. Average rainfall intensity and infiltration rate model (average of 20 years data).
Note: I is the infiltration rate in meter/second, and t is the time in seconds.

Soil Properties

Stiffness and Strength Properties

The elastic and plastic behaviors of Layer-1 and Layer-3 were obtained from the numerical calibration of the CD test results. The calibration was conducted using a single element in an axisymmetric condition. The element was confined by a cell pressure before a strain-controlled load was applied at the top boundary. The resulting deviatoric stress versus the axial strain was plotted and matched with CD test results. Figure 12 presents the results of the numerical calibration. The calibrated elastic parameters, which are K_B and β , and plastic parameters, which are the peak shear strength parameters, are presented in Table 1. A satisfactory result was obtained except around the segment close failure. While the real soils showed elastoplastic hardening, the numerical result was a straight line showing linear elasticity. The inconsistency was introduced as the result of the adopted constitutive model.

The strain softening behavior of Layer-3, which is shown in Figure 12(b), was calibrated by lowering the peak envelope to a critical envelope depending on the amount of plastic shear strain induced. A critical envelope (i.e., so-called fully softened

state) represents an average shear strength at a first-time failure in strain softening soils such as stiff clays (Skempton 1964; Stark et al. 2005). The envelope is perceived to be parallel to the peak envelope but passing through the origin (e.g., Skempton 1964). This means that the peak effective cohesion is degraded while the peak friction angle is kept the same when the soil softens from the peak to the critical state. A linear degradation of effective cohesion was considered, as shown in Equation (9). The expression is given as a function of the plastic deviatoric strain. A similar modeling approach has been adopted by previous studies (e.g., Conte et al. 2010; Lo and Xu 1992; Potts et al. 1997; Zhang et al. 2013).

$$c' = c'_p - (c'_p - c'_{cr}) \frac{\varepsilon_d^p}{\varepsilon_{d,thr}^p} \quad (9)$$

where c' is the degraded effective cohesion due to strain softening [FL^{-2}], c'_p is the peak effective cohesion [FL^{-2}], c'_{cr} is the effective cohesion at a critical state (fully softened state) [FL^{-2}], ε_d^p is the plastic deviatoric strain [dimensionless], and $\varepsilon_{d,thr}^p$ is the threshold plastic deviatoric strain which denotes the shear strain at the critical condition. The best fit shown in Figure 12(b) was obtained when the effective critical cohesion was 1 kPa (close to the origin) and had a threshold plastic deviatoric strain of 10%. Equation (9) was executed using a user-defined code that was based on conditional statements in FLAC, and it was applied to the entire Layer-3 domain.

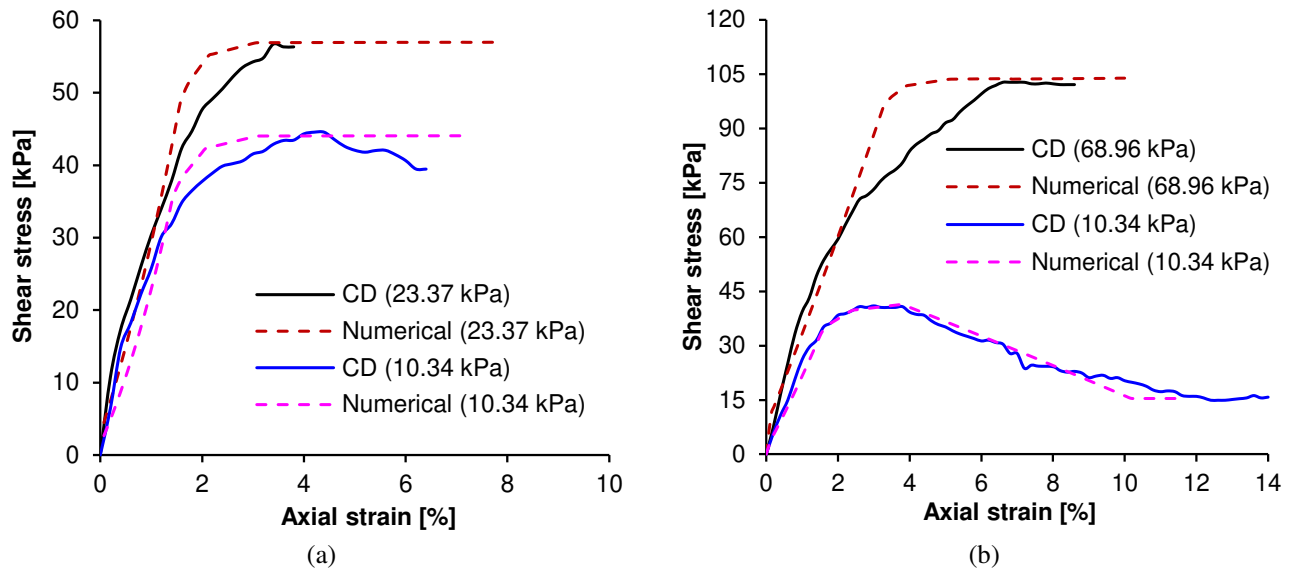


Figure 12. Numerical calibration of the CD test results: (a) Layer-1 and (b) Layer-3.

In addition to the strain softening effect, the shear strength parameters of Layer-3 soils were adjusted for weathering effect. It has been demonstrated that weathering lowers the peak shear strength envelope. However, its explicit effect on effective cohesion and the friction angle is not well researched. Leroueil (2001) has pointed out that weathering has a destructive effect on both particle sizes and interparticle bonds, suggesting that both interparticle friction and cohesion could be affected. In this study, an equal weathering induced degradation was applied on both the effective cohesion and the friction angle (e.g., Conte et al. 2010) as follows:

$$c'(t) = SR_w \times (c'_p \text{ or } c') \text{ and } \tan \phi'(t) = SR_w \times \tan \phi' \quad (10)$$

where $c'(t)$ and $\tan \phi'(t)$ are the effective cohesion and friction angle at a specific time t ; SR_w is the strength reduction associated with weathering and is always less than or equal to 1; and $(c'_p \text{ or } c')$ means c'_p is used if the soil element is not in a strain softening state, and c' is used if the soil element is in a strain softening state. The time variation of SR_w was obtained from Bitar (2020) using a hyperbolic fitting model, as shown in Figure 13. In this Figure, it is noted that one laboratory cycle of weathering was taken equivalent to a one-year weathering effect for the purpose of simplicity.

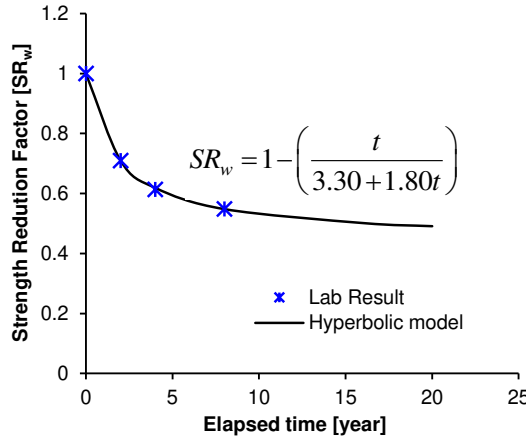


Figure 13. Weathering-induced strength degradation using a hyperbolic model (note: t is in years).

The elastic modulus of Layer-2 soils was estimated from an empirical correlation shown in Equation (11) (Das and Sivakugan 2018; Kulhawy and Mayne 1990):

$$E = \frac{d}{cD_{50}^a} q_c \quad (11)$$

where E is the elastic modulus [MPa]; q_c is the cone tip resistance [MPa]; D_{50} is the particle size corresponding to 50% finer [mm]; $d, c, \& a$ are empirical fitting parameters such that $d = 5$ for sands with fines, while c and a are 5.44 and 0.26, respectively (Kulhawy and Mayne 1990). The cone tip resistance of layer-2 is 14 MPa and D_{50} is referred as 0.43 mm from the gradation curve. Substituting the above values into the equation, the elastic modulus was computed as 16 MPa. The bulk modulus number, K_B , of Layer-2 is then computed as follows:

$$K_B = \frac{E}{3(1-2\nu)} \frac{1}{p_{ref}} \quad (12)$$

where ν is the Poisson's ratio. Assuming a Poisson's ratio of 0.30, the bulk modulus number is estimated as 133. The bulk modulus exponent β was assumed as 0.5, which is typical for sands (Fellenius 2015). The Elastic parameters of Layer-2 are shown in Table 1. Moreover, the plastic behavior of Layer-2 was estimated from CPT results. The effective friction angle of the soil was obtained from the cone tip resistance using the expression shown in Equation (13) (Bowles 1996). Accordingly, the effective friction angle for Layer-2 was found to be 28°.

$$\phi' = 24 + \sqrt{q_c} \quad (13)$$

Hydraulic Properties

The saturated hydraulic conductivity of Layer-3 soils was determined from a specimen under a constant head permeability test (ASTM International D5084 2003). The specimen was saturated before conducting the experiment. A back pressure of 425 kPa was supplied to the sample to ensure acceptable saturation. Then, an influent pressure of 450 kPa was applied, which means that the differential pressure was 25 kPa. The test was run for 15 minutes where the inflow and outflow volume rates were almost similar. With a known pressure gradient and average flow rate, the average saturated hydraulic conductivity of the soil was determined as 4.84×10^{-8} m/s.

The saturated hydraulic conductivity of Layer-1 and Layer-2 soils were estimated from their textural classifications using a database provided by UNSODA (The UNsaturated SOil hydraulic DAtabase) (Leij et al. 1996). Layer-1 soils are loam, while Layer-2 soils are sands. For these textures, the typical saturated hydraulic conductivity of 2.88×10^{-6} m/s and 8.25×10^{-5} m/s were assigned (Leij et al. 1996; Tuller et al. 2004). Values of the van Genuchten parameters and the residual degree of saturation of each layer were obtained based on the typical values corresponding to the textural classification as reported in Leij et al. (1996) and Tuller et al. (2004), and are shown in Table 1.

Table 1. Soil property parameters and their corresponding values.

Parameter	Unit	Soil Layer		
		Layer-1	Layer-2	Layer-3
Dry density, ρ	kg/m ³	1325	1330	1450
Specific gravity, G_s	dimensionless	2.66	2.65	2.69
Porosity, n	dimensionless	0.51	0.50	0.46
Saturated Hydraulic conductivity, k_{sat}	m/s	2.88x10 ⁻⁶	8.25x10 ⁻⁵	4.84x10 ⁻⁸
van Genuchten parameter, α	1/kPa	0.25	0.35	0.35
van Genuchten parameter, n	dimensionless	1.32	3.13	2.00
Initial saturation above GWT	dimensionless	0.41	0.10	0.10
Residual saturation, s_r	dimensionless	0.083	0.058	0.074
Bulk modulus number, K_B	dimensionless	175.00	133.00	55.00
Bulk modulus exponent, β	dimensionless	0.75	0.50	0.25
Poisson's ratio, ν	dimensionless	0.20	0.30	0.35
Peak effective cohesion, c'_p	kPa	12.50	0.00	10.50
Peak effective internal friction angle, ϕ'_p	degree	18.50	28.00	20.20
Critical effective cohesion, c'_{cr}	kPa	-	-	1.00
Threshold plastic deviatoric strain, $\varepsilon_{p,thr}^d$	dimensionless	-	-	0.10

Numerical Modeling Results

Initial Conditions

Figure 14 shows the initial conditions assumed in the numerical simulation. The vertical stress distribution is shown in Figure 14(a) and was governed by the self-weight of the soil materials and groundwater. The initial degree of saturation above the groundwater table dictated the distribution of the initial pore pressure based on the SWCC model, as shown in Figure 14(b). The pore pressure distribution was hydrostatic below the GWT. The shear stress distribution is shown in Figure 14(c). The magnitude of shear stress increased going from the left boundary (where there is no cut section) towards the slope (where there is a cut section). The initial displacement was almost negligible, as shown in Figure 14(d).

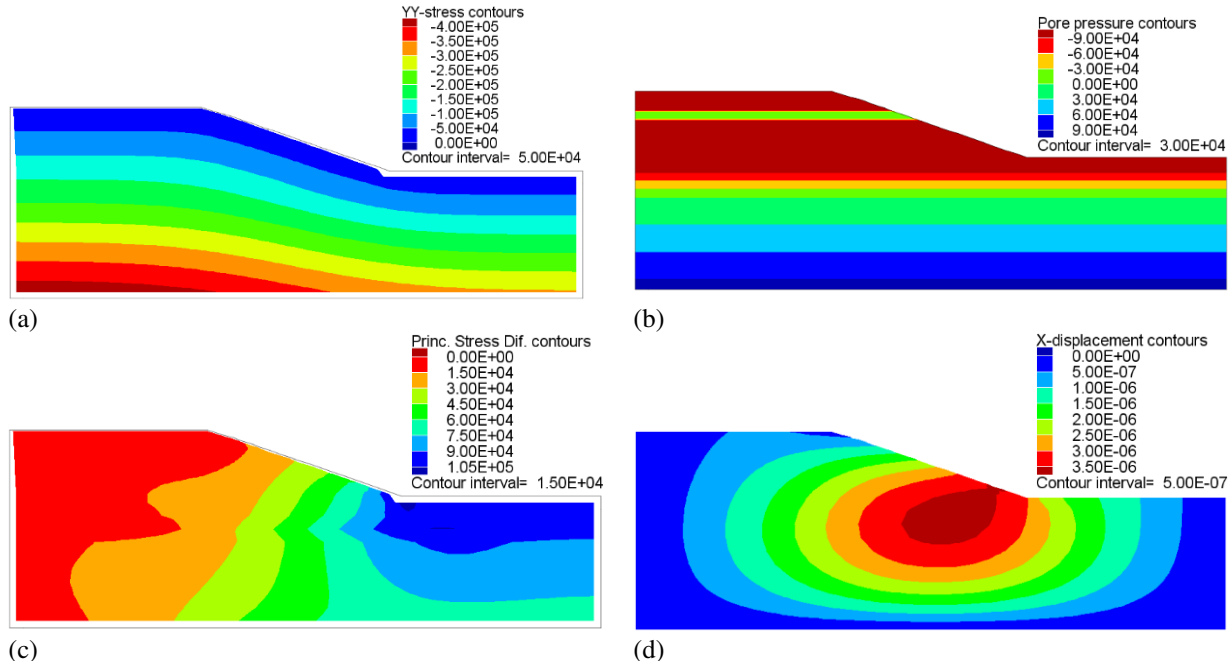


Figure 14. Initial conditions: (a) vertical stress, (b) pore pressure, (c) maximum shear stress, and (d) horizontal displacement (note: unit of stresses is Pa and unit of displacements is m in the contours).

Propagation of the Slip Surface and Deformation at General Failure

The gradual propagation of the slip surface at different time spans is depicted in Figure 15. The time shown under each figure is a numerical time scale. The potential slip surface is indicated by the localization of accumulated maximum shear strain, as shown in the contour plots. Initially, the shear strain was localized to the toe of the slope, where there is potentially maximum shear stress. As time went on, the localized shear strain further developed into a shear band projecting away from the toe. At the end of the 48th month, the slip surface showed a tendency to rotate upward towards the crest direction. Then, it continued its growth over time as shown in the 60th and 65th-month plots.

The development of the slip surface was more gradual in the beginning. However, it became spontaneous and fully developed in a matter of days, as shown in the last two plots of Figure 15. The maximum rate was observed during the maximum rainfall period (where 66 months means 5 Years + ½ Year). This finding suggested that in the presence of substantial strength loss due to other factors such as strain softening and weathering, rainfall could accelerate the rate of failure.

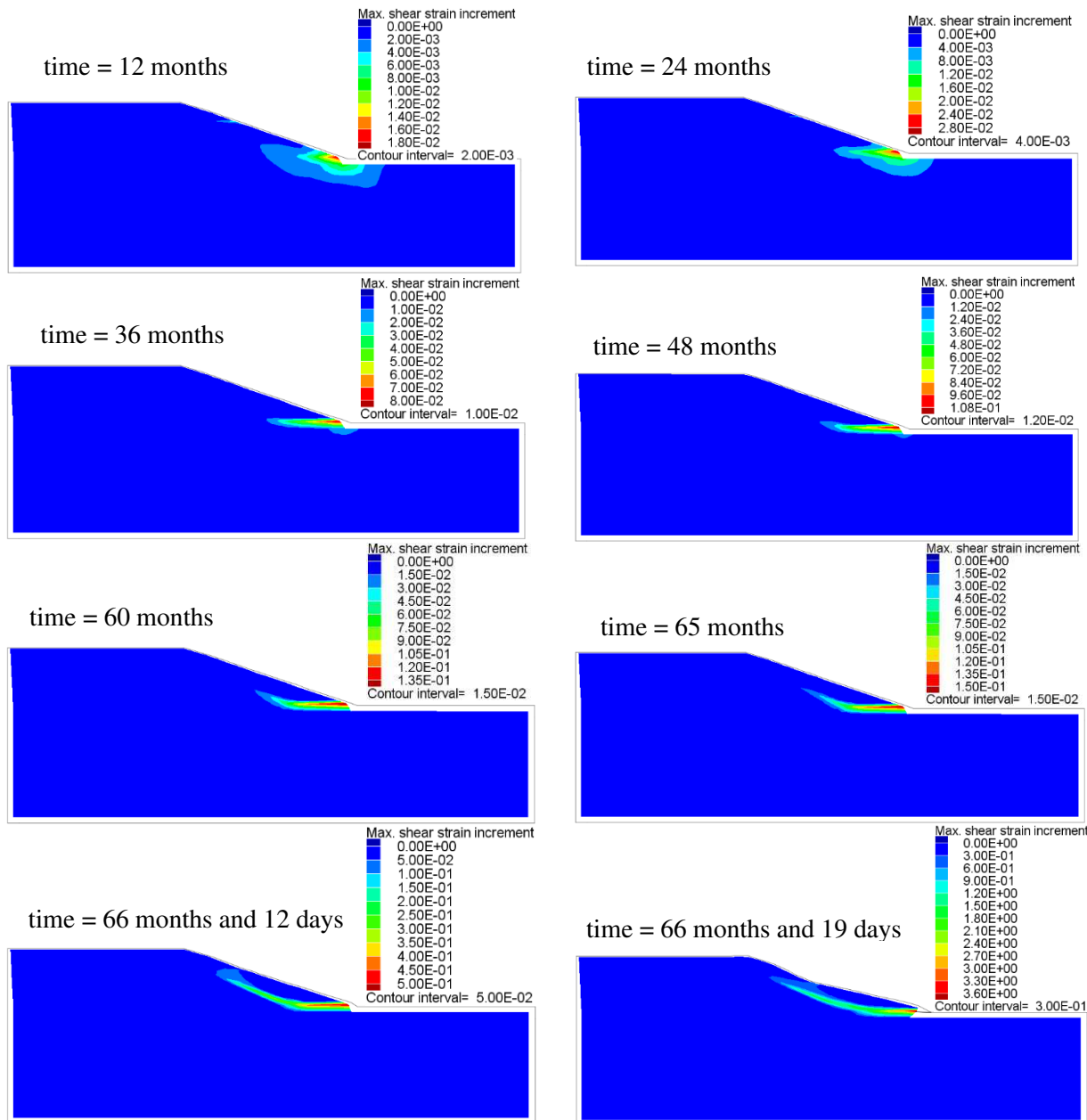


Figure 15. Progressive development of the slip surface with simulation time.

Figure 16 shows the deformation of the slope after the slip surface has fully developed. The maximum horizontal displacement was observed at the toe of the slope. There was a maximum horizontal displacement of 3.85 m as shown in the figure. On the other hand, the maximum vertical displacement (subsidence) was observed on the surface of the slope where the magnitude was 1.32 m. The location of the maximum vertical displacement was in line with the location of the crown of the failure zone observed in the field.

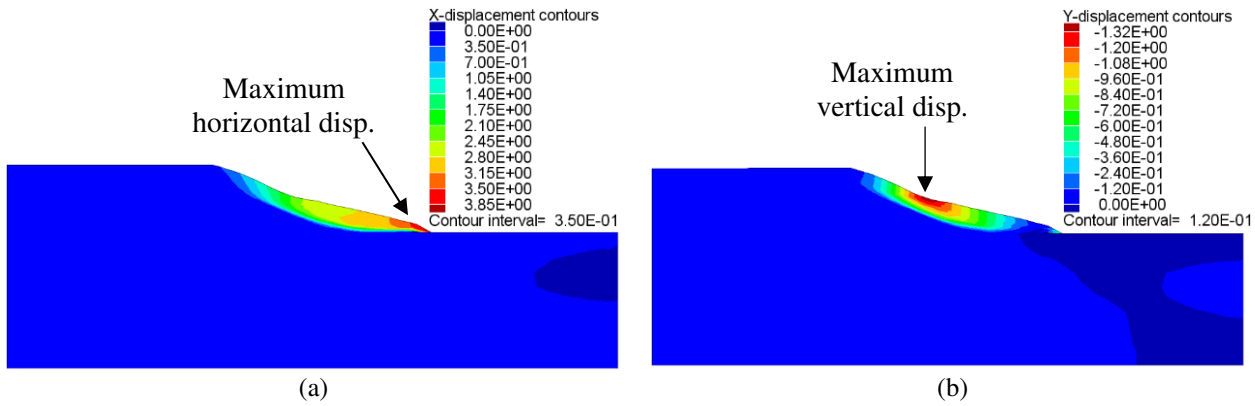


Figure 16. Displacement contours of the slope at general failure: (a) horizontal displacement and (b) vertical displacement. (Note: x-displacement is horizontal displacement, and y-displacement is vertical displacement. Unit of the contour plots is in meters.)

Effects of Strain Softening, Weathering, and Rainfall Infiltration

An evaluation was conducted to understand the effects of strain softening, rainfall, and weathering on the degradation of effective cohesion, the friction angle, and the local factor of safety. Three sensor points were selected along the slip surface, as shown in Figure 17.

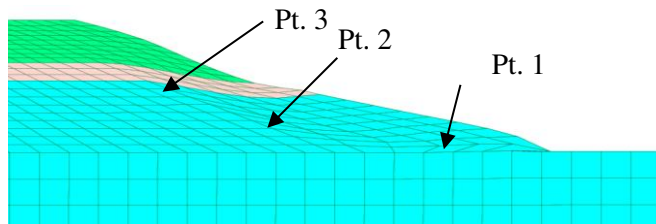


Figure 17. Sensor points chosen for the numerical evaluations.

Figure 18(a) presents the progressive degradation of effective cohesion with time. Pt. 1 showed a relatively rapid degradation of effective cohesion. The reason for this could be the fact that there was a higher shear stress concentration around the toe of the slope, which led to the initiation of strain softening at Pt. 1 earlier than the other two points. On top of that, the additional effect of weathering speeded up the degradation at Pt. 1. On the other hand, Pt. 2 and Pt. 3 showed a degradation of effective cohesion which closely matched the weathering effect up to around the 40th month.

After that, Pt. 2 started to show faster degradation of effective cohesion since the progressive failure had been reached and the effect of all factors was active at that point. Pt. 3 had almost shown a weathering effect until the complete failure of the slope. The strain softening effect was so rapid that the effective cohesion dropped from around 7 kPa to the critical state almost spontaneously. The development of rainfall infiltration (i.e., loss of apparent cohesion) can be clearly seen in regions where there was a stepwise degradation of effective cohesion, as shown in Figure 18(a). Moreover, the effect of rainfall on the strain softening behavior seemed to be more prominent after periods of intense rainfall (hump of the rainfall infiltration function).

The degradation of the effective friction angle's contribution to the failure of the slope was equally important. Figure 18(b) shows the degradation of the effective friction angle. The degradation closely followed the hyperbolic model, which was used

to model the weathering effect. In fact, the effective friction angle was made to degrade based on weathering, while the impact of strain softening was ignored based on the calibration of CD results. The time-dependent degradation of the friction angle had a direct implication on the degradation of the cohesion, because it is their collective effect that caused the weakening of soil elements locally and the progression of strain-softening (the degradation of cohesion). Therefore, a very slow degradation of the effective friction angle (or slow process of weathering) could also slow down the progression of strain softening and the overall progressive failure of the slope.

Perhaps the time it took for the slope to fail, i.e., 32–33 years, means that the process was most probably much slower than the numerical timeframe. The global failure was induced when the effective friction angle reached around 12°, which is much lower than the slope inclination (18.43°) as well as the initial peak effective friction angle (20.2°). Perhaps based on a numerical back analysis, Song et al. (2019) reported that there must be a substantial shear strength degradation at the time of failure for slopes in eastern Nebraska.

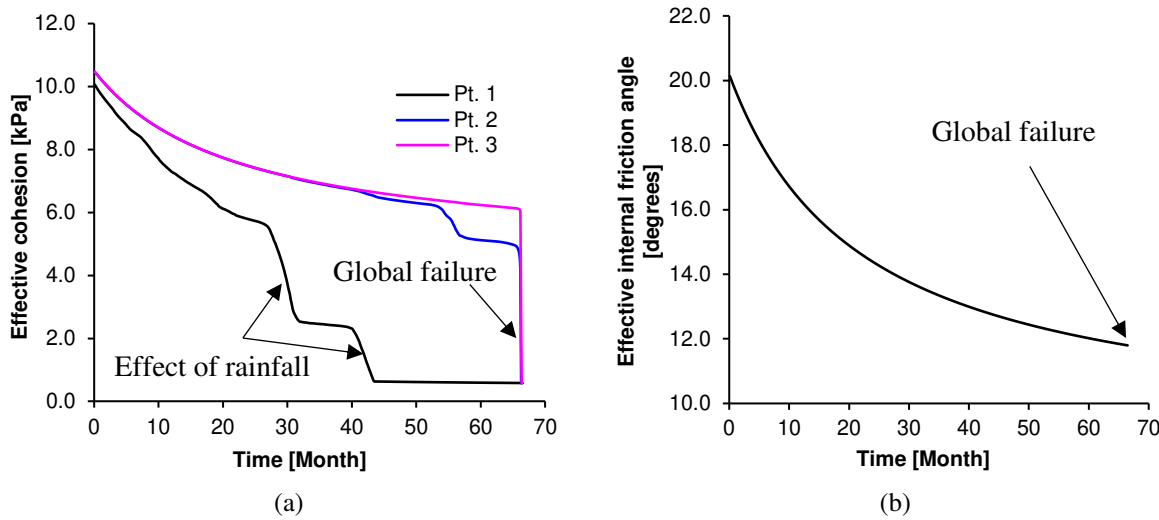


Figure 18. Reduction of shear strength parameters due to softening and weathering: (a) cohesion, and (b) angle of internal friction.

A factor of safety provides a comprehensive slope stability evaluation with just a single number. It includes the effect of confining stress, shear stress, and shear strength parameters in the stability of slopes. Previously, shear strength parameters were evaluated. Here, the local factor of safety is evaluated to understand the overall progression of the failure. A local factor of safety was computed using the expression shown in Equation (14):

$$FS_{local} = \frac{(\sigma'_1 + \sigma'_3) \sin \phi' + 2c' \cos \phi'}{\sigma'_1 - \sigma'_3} \quad (14)$$

where FS_{local} is a local factor of safety [dimensionless]. In the numerator, there are the influences of confining stress and shear strength parameters (both are stabilizing agents), while in the denominator there is the influence of shear stress (destabilizing agent). A critical condition is induced when the ratio becomes 1. Equation (14) was implemented in FLAC using a user-defined function and was executed at each time step. The evolution of the local factor of safety at the selected three sensor points is shown in Figure 19.

The initial local factor of safety was already close to 1 for Pt. 1. This means that the point was locally under critical condition. The initial local factor of safety for Pt. 2 and Pt. 3 was higher than 1, suggesting both elements were safe against failure. But as time progressed, the local factor of safety lessened in both Pt. 1 and Pt. 2. Pt. 3 showed a faster reduction of the factor of safety than Pt. 2 up to around the 12th month despite the fact that their shear strength parameters degraded equally, as shown in Figure 18.

Upon evaluation, it turned out that the effect of rainfall had caused Pt. 3 to lose more of its suction more rapidly than Pt. 2 due to a faster flow of percolated water near the interface between Layer-2 and Layer-3. Once the majority of the suction was lost and there was little suction variation with time, the factor of safety remained fairly constant for some time before the

effects of strain softening and weathering became more prominent at Pt. 3. After that, even a little variation suction due to seasonal changes substantially reduced the factor of safety. The critical factor of safety progressed from Pt. 1 to Pt. 2 and then to Pt. 3. The global failure happened once all points reach the critical factor of safety. Depending on how slow the weathering process is and how quickly the suction is lost (precipitation-evaporation effects), the rate of strain softening and time for global failure may be substantially different with the numerical time scale.

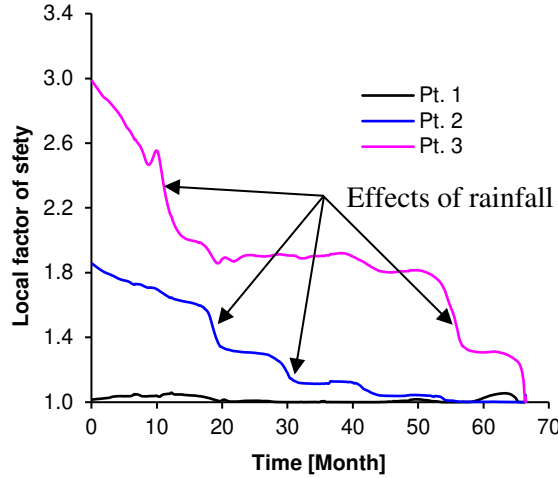


Figure 19. Variation of the local factor of safety at the sensor point.

COMPARISON OF NUMERICAL OUTPUT AND MEASURED DATA

The numerical simulation result was compared with the observations made from LiDAR and field surveying. The comparison was performed on the deformation pattern of the slope surface from the numerical study and field measurements. The numerical surface deformation of the slope was extracted from the time of global failure because this is the condition where the slip surface was fully developed, and significant deformation was observed.

Figure 20 shows the slope surface deformation obtained from the numerical analysis, LiDAR, and field surveying. The numerical result was in close agreement with the measured deformation with some discrepancies. The numerical simulation result tended to overpredict lateral deformation toward the bottom and underpredict deformation toward the top of the sliding mass. The mismatch in the deformation pattern could be due to the inherent difficulty in analyzing large strain behavior without a robust numerical approach and constitutive model that mimic the plastic behavior of Loess (collapsible soils) and strain softening soils.

The Mohr-Coulomb model adequately mimicked the shear strength behavior of the soils, as seen from the calibration of the laboratory tests. However, it may not be sophisticated enough to incorporate the hardening and plastic flow behavior of soils such as those described in the critical state soil mechanics. From the observation of the surface deformation from the numerical analysis, it seemed that the sliding body showed excessive stretching when the yield strength became too low due to strength degradation. This stretching may be rectified with the incorporation of a model that can accommodate more sophisticated plasticity.

Moreover, the numerical modeling showed a tendency of crack formation around the crest of the slope through the development of the tension state, as shown in Figure 21(a). Even though there was this tendency, the two zones could not separate due to the employed continuum approach. More subsidence might have been observed if the separation was allowed by using a more robust numerical approach.

Based on the overall examination through both the measured observations and the numerical analysis, a qualitative engineering explanation is given to the failure condition in Figure 21(b). It is more likely that the failure was triggered by Layer-3 soils. The propagation of the local slip surface was gradual, as learned from the history of the slope. A global failure was triggered when the slip surface reached Layer-2. Due to the subsequent sliding of both Layer-1 and Layer-2, a portion of Layer-1 lost its bottom support, and a tension crack was formed. Through this tension crack, rainwater could have migrated

and induced the collapse of the loess and the formation of the scarp. The addition of fill materials will increase the weight of the unstable zone, and the slope will repeat the sliding mechanisms unless the mitigation work traverses the slip surface.

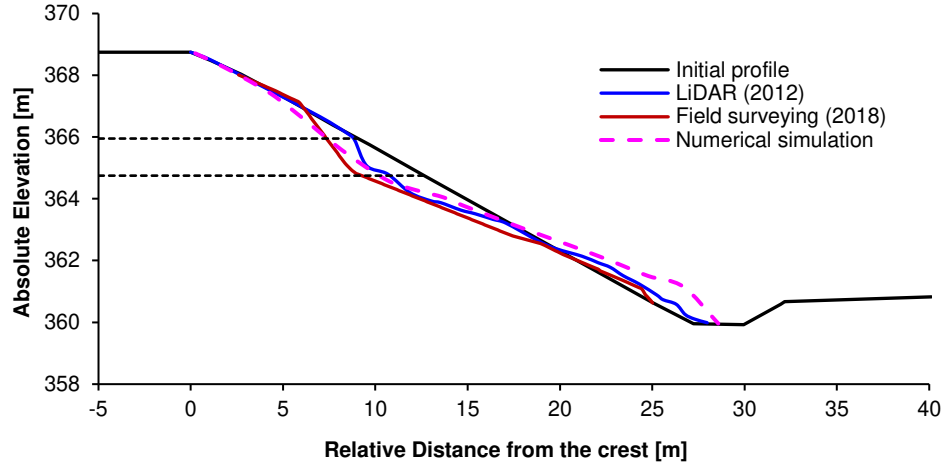


Figure 20. Comparison of slope profile from LiDAR, ground surveying, and numerical study

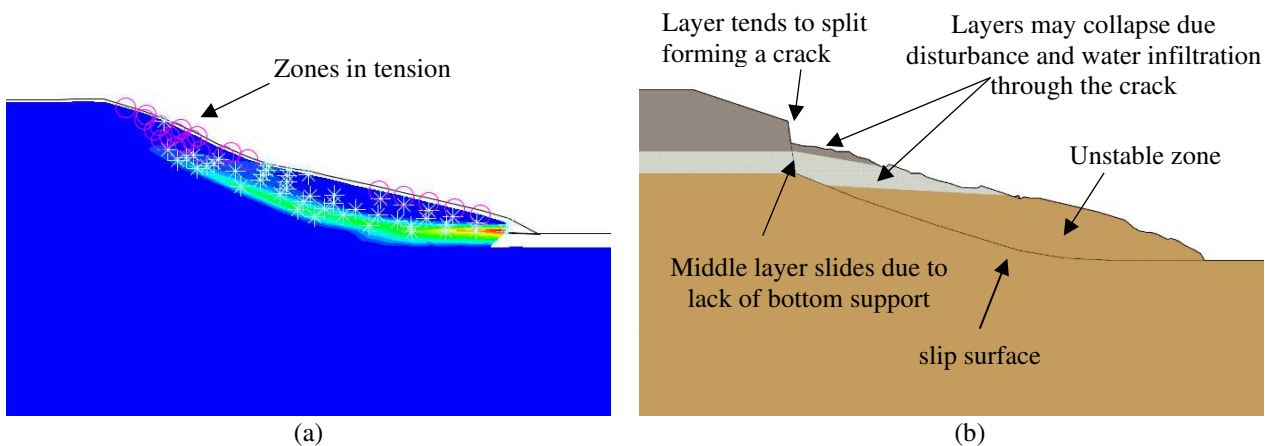


Figure 21. (a) States of different zones in the vicinity of failure indicating the possible location of crack (note: circles indicate tensioned zones and stars indicate sheared zones), and (b) qualitative explanation of the failure condition.

SUMMARY AND CONCLUSIONS

This study presented a case history on a failed slope located in Lincoln, NE. A failure was observed although the slope was shallow. The slope material behavior was evaluated to understand the contributing factors for the failure. The geotechnical investigation through a CD triaxial test revealed that the bottom soil layer exhibited strain softening behavior. In addition, a different study on a similar soil type (of similar geological formation and location) showed the soil was susceptible to degradation of strength due to weathering. Since the effect of water cannot be overlooked, a rainfall infiltration was taken into account in the evaluation of the slope failure. With the anticipated failure factors, a numerical investigation was carried out to further understand the progressive evolution of the slip surface and the local factor of safety.

A transient hydromechanical coupled simulation was performed using FLAC2D. The elastic, plastic, and hydraulic parameters were obtained by a calibration of CD tests and empirical correlations. The rainfall effect was simulated assuming an average yearly fluctuation of infiltration rate from 20 years rainfall record. The pertinent failure mechanisms were all incorporated through the use of user-defined functions in FLAC. The plastic shear strain propagation showed that the slip surface was developing progressively. Evaluation of the effective cohesion, effective friction angle, and local factor of safety showed the apparent effects of strain softening, weathering, and rainfall infiltration on the slope. The failed slope profile



from the numerical simulation closely agrees with the measured profile from LiDAR and field surveying. The numerical simulation had effectively demonstrated how strength degradation due to several factors may lead to progressive failure of slopes. Finally, the study made the following conclusions:

- The nature of subsoils needs to be investigated and properly modeled to understand the mechanisms of progressive failure and design resilient slopes.
- The potential occurrence of strain softening and weathering should be checked, and a numerical deformation analysis carried out during the design of slopes containing glacial tills.
- In addition, it is noted that unstable mass beneath loess formations could lead to disturbances and ultimate collapse.
- The formation of cracks could contribute to the enhanced infiltration of water, leading to the collapse.
- In the presence of substantial strength loss by other means, rainfall had a potential implication in terms of accelerating the progression of failure. Therefore, it should be accounted for in the slope stability evaluation.

ACKNOWLEDGMENTS

The authors of this study express their appreciation to the Nebraska Department of Transportation for financial support with research grants 26-1121-4042-001 and 26-1121-4052-001. Technical help from Mr. Nikolas Glennie and Alex Silvey is particularly appreciated

REFERENCES

Alonso, E., and Pineda, J. (2006). "Weathering and degradation of shales: experimental observations and models of degradation." *VI South American Rock Mechanics Conference*, Cartagena de Indias, Colombia.

Arthur Bettis, E., Muhs, D. R., Roberts, H. M., and Wintle, A. G. (2003). "Last Glacial loess in the conterminous USA." *Quaternary Science Reviews*, Loess and the Dust Indicators and Records of Terrestrial and Marine Paleoenvironments (DIRTMAP) database, 22(18), 1907–1946.

ASTM International D698. (2012). *Test Methods for Laboratory Compaction Characteristics of Soil Using Standard Effort (12 400 ft-lbf/ft³ (600 kN·m/m³))*. ASTM International.

ASTM International D3080. (2004). *Test Method for Direct Shear Test of Soils Under Consolidated Drained Conditions*. ASTM International.

ASTM International D4318. (2017). *Test Methods for Liquid Limit, Plastic Limit, and Plasticity Index of Soils*. ASTM International.

ASTM International D5084. (2003). *Test Methods for Measurement of Hydraulic Conductivity of Saturated Porous Materials Using a Flexible Wall Permeameter*. ASTM International.

ASTM International D6913. (2017). *Test Methods for Particle-Size Distribution (Gradation) of Soils Using Sieve Analysis*. ASTM International.

ASTM International D7181. (2011). *Test Method for Consolidated Drained Triaxial Compression Test for Soils*. ASTM International.

ASTM International D7928. (2017). *Test Method for Particle-Size Distribution (Gradation) of Fine-Grained Soils Using the Sedimentation (Hydrometer) Analysis*. ASTM International.

Bishop, A. W. (1959). "The principle of effective stress." *Teknisk ukeblad*, 39, 859–863.

Bitar, L. (2020). *Optimum Mixing Design of Xanthan and Gellan Treated Soils for Slope Stabilization for Weathered Shales and Glacial Tills in Nebraska*, Master's Thesis, University of Nebraska-Lincoln, Lincoln, NE.

Botts, M. E. (1998). "Effects of slaking on the strength of clay shales: A critical state approach." *Geotechnics of hard soils–soft rocks* (ed. A. Evangelista), 1, 447–458.

Bowles, J. E. (1996). *Foundation analysis and design*, McGraw-Hill, New York.

Carse, L. A. (2014). *The geomechanical response of cut slopes in glacial till to climatically driven pore-pressure cycling and hydrogeology*, PhD Thesis, Queen's University Belfast.

Conte, E., Silvestri, F., and Troncone, A. (2010). "Stability analysis of slopes in soils with strain-softening behaviour." *Computers and Geotechnics*, 37(5), 710–722.

Dagger, R., Saftner, D., and Mayne, P. (2018). *Cone Penetration Test Design Guide for State Geotechnical Engineers*, Minnesota Department of Transportation, St. Paul, Minnesota, 225.



Darban, R., Damiano, E., Minardo, A., Olivares, L., Picarelli, L., and Zeni, L. (2019). "An Experimental Investigation on the Progressive Failure of Unsaturated Granular Slopes." *Geosciences*, Multidisciplinary Digital Publishing Institute, 9(2), 63.

Das, B. M., and Sivakugan, N. (2018). *Principles of Foundation Engineering*, Cengage Learning, Boston, MA.

Eversoll, D. A. (2013). "Landslides of Nebraska." *Conservation and Survey Division, School of Natural Resources, Institute of Agricultural and Natural Resources University of Nebraska-Lincoln*, 24.

Fellenius, B. H. (2015). *Basics of Foundation Design*. www. Fellenius.com.

Itasca Consulting Group, Inc. (2019). *Fast Lagrangian Analysis of Continua*, Minneapolis, MN.

Kulhawy, F. H., and Mayne, P. W. (1990). *Manual on estimating soil properties for foundation design*, Electric Power Research Institute, Palo Alto, CA; Cornell University, Ithaca, NY.

Leij, F. J., Alves, William J., and van Genuchten, Martinus Th. (1996). *The UNSODA unsaturated soil hydraulic database: user's manual*, National Risk Management Research Laboratory, Office of Research and Development, Cincinnati, OH.

Leroueil, S. (2001). "Natural slopes and cuts: movement and failure mechanisms." *Géotechnique*, 51(3), 197–243.

Lo, S.-C. R., and Xu, D.-W. (1992). "Short Term Stability of Reinforced Embankment on Soft Clay: Modelling of Strain Softening and Reinforcement Extensibility." *Soils and Foundations*, 32(1), 189–204.

Lu, N., and Likos, W. J. (2004). *Unsaturated soil mechanics*, Wiley, New York.

Mesri, G., and Shahien, M. (2003). "Residual Shear Strength Mobilized in First-Time Slope Failures." *Journal of Geotechnical and Geoenvironmental Engineering*, 129(1), 12–31.

Parsons, R. L., Johnson, R. M., Brown, D. A., Dapp, S., and Brennan, J. J. (2009). "Characterization of loess for deep foundations." *DFI Journal-The Journal of the Deep Foundations Institute*, 3(2), 14–24.

Potts, D. M., Kovacevic, N., and Vaughan, P. R. (1997). "Delayed collapse of cut slopes in stiff clay." *Géotechnique*, 47(5), 953–982.

Rahardjo, H., Leong, E. C., Deutscher, M. S., Gasmo, J. M., and Tang, S. K. (2000). *Rainfall-induced slope failures*, NTU-PWD Geotechnical Research Centre, Nanyang Technological University.

Skempton, A. W. (1964). "Long-Term Stability of Clay Slopes." *Géotechnique*, 14(2), 77–102.

Song, C. R., Bahmyari, H., Bitar, L., and Amelian, S. (2019). *Nebraska Specific Slope Design Manual*, Nebraska Transportation Center; Nebraska Department of Transportation, Lincoln, NE.

Song, C. R., Bekele, B., Silvey, A., Lindemann, M., and Ripa, L. (2020). "Piezocone/cone penetration test-based pile capacity analysis: calibration, evaluation, and implication of geological conditions." *International Journal of Geotechnical Engineering*, 1–14.

Stark, T. D., Choi, H., and McCone, S. (2005). "Drained shear strength parameters for analysis of landslides." *Journal of Geotechnical and Geoenvironmental Engineering*, 131(5), 575–588.

Sullivan, W. G., Howard, I. L., and Anderson, B. K. (2015). "Development of Equipment for Compacting Soil-Cement into Plastic Molds for Design and Quality Control Purposes." *Transportation Research Record*, 2511(1), 102–111.

Take, W. A., and Bolton, M. D. (2011). "Seasonal ratcheting and softening in clay slopes, leading to first-time failure." *Géotechnique*, 61(9), 757–769.

Tuller, M., Or, D., and Hillel, D. (2004). "Retention of water in soil and the soil water characteristic curve." *Encyclopedia of Soils in the Environment*, 4, 278–289.

UNL. (2020). "Lincoln, NE Climate Data | Lincoln Weather and Climate | Nebraska." <<https://lincolnweather.unl.edu/data>> (Nov. 25, 2020).

Van Genuchten, M. T. (1980). "A closed-form equation for predicting the hydraulic conductivity of unsaturated soils." *Soil science society of America journal*, 44(5), 892–898.

Zhang, K., Cao, P., and Bao, R. (2013). "Progressive failure analysis of slope with strain-softening behavior based on strength reduction method." *Journal of Zhejiang University Science A*, 14(2), 101–109.



INTERNATIONAL JOURNAL OF
**GEOENGINEERING
CASE HISTORIES**

*The Journal's Open Access Mission is
generously supported by the following Organizations:*



Geosyntec
consultants

engineers | scientists | innovators

CONETEC



ENGEO
Expect Excellence

Access the content of the ISSMGE International Journal of Geoengineering Case Histories at:
<https://www.geocasehistoriesjournal.org>